Observations of Small-scale Magnetic Flux Ropes Associated With Significant Values of Partial Variance Increment Indices

Yu Chen[1] and Qiang Hu[1,2]

[1]Center for Space Plasma and Aeronomic Research (CSPAR), The University of Alabama in Huntsville, Huntsville, AL 35805, USA
[2]Department of Space Science, The University of Alabama in Huntsville, Huntsville, AL 35805, USA

Key Points:

- Around 3% of SFRs identified by the Grad-Shafranov-based detection could be indiscernible from the current sheet structures.
- Large PVI values in SFRs mostly correspond to boundary current sheets, field-line kinks, and a rotational discontinuity near the center.
- Multi-point spacecraft measurements are necessary to distinguish SFRs from other structures with magnetic field rotations.

Corresponding author: Qiang Hu, `qh0001@uah.edu`

Abstract

We report recent findings for the magnetic field configurations of small-scale magnetic flux ropes (SFRs) broadly defined and identified by using the Grad-Shafranov-based techniques for in-situ measurements via the Parker Solar Probe (PSP), Solar Orbiter (SolO), and two Helios spacecraft. Since the current sheets were found to occur at boundaries of SFRs and/or inside SFRs at 1 AU via the partial variance increment (PVI) and the Grad-Shafranov (GS) reconstruction technique by Pecora et al. (2019), we further examine such a co-existence in this study by assessing the maximum PVI indices within SFR intervals using the above four spacecraft observations throughout the inner heliosphere ($\leqslant$1 AU). Less than 15% of SFRs have maximum PVI indices exceeding a threshold value of 6 that is used to indicate a current sheet structure. Three representative events are selected to explain the most common situations. (1) Current sheets occur at SFR boundaries and near the center. Each could be a weak switchback feature in the time-series profile of the gradually bipolar magnetic field rotations. (2) An SFR configuration is confirmed by both the measurement of counterstreaming electrons and the GS reconstruction result, despite that a large PVI value occurs near the SFR center which is due to an arbitrary kink instead of a current sheet. (3) A current sheet is falsely identified as an SFR where a significant PVI value ($\sim$7) occurs near the center. In the end, we discuss the necessity of using multi-point spacecraft measurements to discern the structures associated with SFRs.

1 Introduction

Magnetic flux ropes, in the shape of bundled twisted magnetic field lines, have been investigated over several decades. The intrinsic characteristics of interplanetary magnetic flux ropes, based on in-situ spacecraft observations, have been revealed using analytic model fitting (e.g., Choi et al., 2022; Hu, He, & Chen, 2022) and the two-dimensional (2D) Grad-Shafranov (GS)-based detection technique (Hu et al., 2018). The large-scale flux ropes, also known as magnetic clouds, can be studied via remote sensing and in-situ observations (e.g., Hu, Zhu, et al., 2022). They possess significantly large sizes and are associated with coronal mass ejections (CMEs). On the other hand, the small-scale magnetic flux ropes (hereafter, SFRs), whose sizes are down to a few hundred kilometers, have been suggested to form part of the "spaghetti-like structured solar wind" together with presumably non-twisted flux tubes (Borovsky, 2008). These relatively small-scale structures were observed to be omnipresent from the region near the Sun to regions at different heliocentric distances and heliographic latitudes. Sometimes, they occur within large-scale solar wind structures such as stream interaction regions and near the heliospheric current sheet (Chen & Hu, 2020; Choi et al., 2022; Chen et al., 2023). Their properties such as duration and scale size are found to follow power-law and log-normal distributions, and they possess mid to high Alfvénicity at small distances in the slow solar wind and in high-speed winds at higher latitudes (Farooki, Noh, et al., 2024; Farooki, Lee, et al., 2024; Chen et al., 2019). Overall, SFRs occur much more frequently than magnetic clouds, and there is no clear separation of the two distinct populations in the distributions of all their relevant properties. In addition, the GS-based detection algorithm does not separate the magnetic flux ropes based on their scale sizes. Therefore, to be consistent with all our previous studies, we use the term "SFR" throughout this study without confining our event candidate to be "small" in duration or size.

Current sheet is also a common type of structure occurring in the solar wind (Miao et al., 2011; Phan et al., 2020; J. Huang et al., 2023). The well-known largest structure is the heliospheric current sheet (HCS), which shows clear signatures such as changes in magnetic field polarities, enhanced proton number density and plasma beta, etc., as a spacecraft passes across, typically accompanied by a break in the electron pitch angle distribution for the electron streaming along the magnetic field lines. Identification of smaller-scale current sheets using solar wind spacecraft measurements often focuses on sudden changes in the magnetic field directional angles and/or the field components between two adjacent timestamps (Li, 2008; Greco et al., 2009). Sometimes, current sheets are identified together with reconnection exhaust, i.e., a region bounded by bifurcated current sheets (Runov et al., 2003). They usually consist of two rotational discontinuities (RDs). In a time-series plot obtained from a spacecraft across a bifurcated current sheet, one can see pairs of correlated magnetic field components with the velocity counterparts on one side and anti-correlated pairs on the other. When these observational signatures occur, they are also identified as "reconnecting current sheets" (Phan et al., 2006, 2009; Teh et al., 2009). For these reconnecting current sheets, the Alfvénic plasma jet will show up in the outflow region in addition to the topological change of the magnetic field, due to the correspondence of active magnetic reconnection (Gosling et al., 2005; Davis et al., 2006).

The aforementioned three types of structures, i.e., SFRs, current sheets, and magnetic reconnection exhaust, are considered to be related, especially in either 2D or 3D simulations of the magnetohydrodynamics (MHD) turbulence. Reconnected field lines at the current sheet may generate magnetic islands in outflow regions (Greco et al., 2009). Furthermore, current sheets could form magnetic walls of SFRs simultaneously (Miao et al., 2011; Zheng & Hu, 2018). However, in the 1D time-series data, both SFRs and current sheets are recognized according to magnetic field rotations depending on the data resolution. A sudden change in field components could exist in a longer interval that also may exhibit gradually bipolar field rotations. Under this circumstance, structures for a current sheet structure and a typical SFR may be intermixed, leading to ambiguity in distinguishing these structures. Also, both are occasionally accompanied by enhanced magnetic field strength (e.g., Fargette et al., 2021), which thus brings challenges in distinguishing between SFRs and current sheets, especially for single-spacecraft measurements.

To address this issue, Pecora et al. (2019) combined the GS reconstruction technique with the Partial Variances Increment (PVI) indices to distinguish and quantify the roles of flux ropes and current sheets, especially when they co-exist. They performed GS reconstruction to generate 2D configuration of hundreds of SFRs and identified the locations of relatively large PVI values within each SFR interval. They summarized three categories of events: (1) the X-point type where current sheet(s) exist at boundaries of flux tubes, (2) O-point type where current sheet(s) occur within flux tubes, and (3) neither (N) type events. They found that about half of their events are X type. Note that these analysis results are obtained via the spacecraft observations at 1 AU. With the growing amount of data within 1 AU by both Parker Solar Probe (PSP) and Solar Orbiter (SolO), one may wonder if there is an additional circumstance containing both SFRs and current sheets. First, the SFRs identified via the PSP were found to overlap with the other types of structures, e.g., the magnetic switchbacks (Chen & Hu, 2022). Moreover, these ubiquitous switchbacks were suggested to be stabilized by small-scale current sheets (J. Huang et al., 2023). Thus, it is likely that current sheets, SFRs, and switchbacks co-exist in the same scenario. Meanwhile, the SFR database, at `http://www.fluxrope.info/`, has published over 10,000 events using PSP datasets. Therefore, whether this database contains falsely identified events and if so, how many of them are, has always puzzled us.

In this study, we present the recent investigation of SFRs especially their association with current sheets, using the GS-based detection results from the PSP, SolO, and Helios 1 & 2 in-situ measurements. This paper is organized as follows. Section 2 briefly introduces the GS-based detection method, the calculation of the PVI, the four spacecraft datasets, and specific data processing details. In Section 3, we first present the overview of SFRs via the four missions, such as distributions of selected parameters for these SFRs. Moreover, we dive into those SFRs associated with large PVI indices with both statistical and individual case studies. Three typical events are selected to represent the most common circumstances. Finally, we summarize our major findings in Section 4 and discuss the future work.

2 Method and Data

The identification of SFRs is through the extended GS-based detection algorithm (Zheng & Hu, 2018; Hu et al., 2018; Chen & Hu, 2022). It relies on the GS-type equation (Sonnerup et al., 2006; Teh, 2018):

$$\nabla^2 A = -\mu_0 \frac{dP_t}{dA} = -\mu_0 \frac{d}{dA}\left[(1-\alpha)^2\frac{B_z^2}{2\mu_0} + (1-\alpha)p + \alpha(1-\alpha)\frac{B^2}{2\mu_0}\right], \tag{1}$$

where the transverse pressure is defined by the terms inside the square brackets, $P_t = [...]$. The scalar function $A(x, y)$ is equivalent to the 2D magnetic flux function, characterizing the cylindrical configuration of the structure with the parameter $\alpha \equiv Const$. Such a configuration has invariance along its axis z, i.e., $\partial/\partial z = 0$. The initial value of A along the projected spacecraft path along $y = 0$ is calculated from the spacecraft measurement, i.e.,

$$A(x, 0) = -\int_0^x (1 - \alpha) B_y(x', 0) dx'. \tag{2}$$

Values of A over a 2D cross-sectional plane are then obtained by solving an initial value problem (see Hu and Sonnerup (2002); Hu (2017) for more details). In the above equation under the assumption that the remaining plasma flow in a frame of reference moving with the SFR is aligned with the magnetic field, the factor $\alpha = \langle M_A \rangle^2 \approx Const$ is the square of the average Alfvén Mach number, which indicates an approximately constant proportionality of the remaining flow speed to the local Alfvén speed. Notice that the equation (1) returns to the traditional GS equation when $\alpha = 0$ (Sonnerup & Guo, 1996; Hau & Sonnerup, 1999).

The GS-based detection algorithm was inspired by the application of the GS reconstruction technique (Hu & Sonnerup, 2000; Hu & Sonnerup, 2001) and makes use of the unique feature described by the GS equation. A spacecraft traversing an SFR structure will record bipolar rotations of the magnetic field, which shows gradual changes in one or more field components reversing signs. In the local flux rope frame, given by the coordinates (x, y, z) for the GS equation, it is typically the B_y component that changes sign. Correspondingly, in the 2D plane perpendicular to the flux rope z-axis, an SFR structure is usually depicted as a series of nested iso-surfaces (contours) of the magnetic flux function A. The aforementioned change of the sign of the B_y component in equation (2) thus corresponds to changes of A from one boundary to the extreme value near the center and to the other boundary returning to its value at the beginning again. The point where A reaches its extreme value is also defined as the turning point. As shown in the equation (1), since P_t is a single variable function of A, one can also expect for an SFR that P_t will follow the same change as A. Therefore, the identification of SFRs is simplified to searching for a double-folding pattern of P_t *versus* A between the inbound and the outbound spacecraft paths traversing a structure. The detailed detection algorithm and associated criteria were described in Hu et al. (2018); Chen and Hu (2022). In short, the basic requirement for the GS-based algorithm is that the function $P_t(A)$ be single-valued and double-folded in an interval. All related quantities for the detection algorithm are obtained from the in-situ single spacecraft data. The related Python package is now available on GitHub at https://github.com/PyGSDR/PyGS and can be accessible via the Python in Heliophysics Community (PyHC) at https://heliopython.org/.

The significant value of the Partial Variance Increment (PVI) index is used to determine the passages of current sheets (Greco et al., 2008; J. Huang et al., 2023) from in-situ spacecraft measurements. It is calculated by using the time-series mangetic field vectors **B**:

$$\mathrm{PVI}_{\mathrm{s},\tau} = \frac{|\Delta\mathbf{B}(\mathrm{s},\tau)|}{\sqrt{\langle|\Delta\mathbf{B}(\mathrm{s},\tau)|^2\rangle}}. \tag{3}$$

The increment $\Delta\mathbf{B}$ is between the field at time s and that after a time lag τ, i.e., $\Delta\mathbf{B}(s,\tau) = \mathbf{B}(s+\tau) - \mathbf{B}(s)$. Here, the time lag $\tau = \Delta t$, the resolution of processed datasets, may have different values as described in the following paragraph. As suggested in J. Huang et al. (2023), the average symbol in the denominator is calculated via an 8-hour window. In this study, we use the criterion, i.e., PVI > 6, to indicate the possible current sheet structure considering that the original data are downsampled for the GS detection.

This study uses four spacecraft datasets from PSP, SolO, and Helios 1 & 2, in order to have rather complete radial distance coverage spanning the inner heliosphere to 1 AU. The magnetic field and plasma bulk parameters of PSP are provided by the FIELDS (Bale et al., 2016) and the Solar Wind Electrons Alphas and Protons (SWEAP, Kasper et al. (2016)) instrument suites. The latter includes both Solar Probe Cup (SPC, Case et al. (2020)) and the Solar Probe Analyzers Ion (SPAN-Ion, Livi et al. (2022)) probes. The SPC data are used in most time periods, and the SPAN-Ion data are to supplement the SPC data around the perihelion when the SPC data with "Only Good Quality" were unavailable. The PSP data are downsampled to 28s cadence when the PSP was under the cruise mode. When it was under the encounter mode (mostly within 0.25 AU), they are processed to the nearest integer cadence in seconds, such as 1s, 4s, etc. The magnetic field data onboard the SolO are from the Magnetometer (MAG, (Horbury et al., 2020)), whereas data of plasma bulk properties are via the Solar Wind Analyzer Suite (SWA, Owen et al. (2020)). The original data resolution is slightly downsampled to 4s. Since the SolO lasts a rather shorter time period since its launch, we also include the results from Helios 1 & 2 "New Proton Corefit Data" (Porsche, 1981; Stansby et al., 2018), which were downsampled to 1 min for the detection. Actually, the SFRs via these two datasets had already been published in Chen and Hu (2020). However, those events were obtained with the original GS equation, which may exclude some intervals with modest Alfvénicity. In this study, we re-processed the SFR candidates detected from Helios 1 & 2 by using the extended GS-type equation (1) and the associated criteria (Chen & Hu, 2022).

3 Results

Table 1. Overview of GS-based SFR detection results for different spacecraft datasets.

Datasets	Time period (UT)	Radial distance (AU)	Duration (s)	Scale size (AU)	V_{sw} (km s^{-1})	Count
PSP[a]	2018 Oct 30-2023 Apr 30	0.062-0.772	10-21,645	1.97×10^{-6}-0.0754	93.70-1607.98	31,541
SolO	2021 Apr 22-2023 Apr 24	0.293-1.015	37-21,645	7.67×10^{-6}-0.0889	215.32-1144.76	8,357
Helios 1 & 2	1975-1984, 1976-1980	0.29-0.985	481-61,621	1.82×10^{-4}-0.19	211.55-1090.3	8,838

[a]PSP datasets include both SPC and SPAN-Ion data.

As aforementioned, the automated detection of SFRs has been carried out for the recent PSP and SolO spacecraft data. The candidates in the previous database using two Helios spacecraft measurements have been reprocessed in this study. Totally over 40,000 events are recognized. Table 1 and Figure 1 present an overview of the detection periods and a summary of the selected SFR properties and detailed distributions of each set of results. The detection of SFRs using the PSP data encompasses a mission period up to Orbit No.15, i.e., from 2018 October 30 to 2023 April 30. These events were discovered at smaller heliocentric distances, i.e., between 0.062 and 0.772 AU. Figure 1(a) shows that the SPC dataset contributes the most to SFR counts at distances less than 0.5 AU. Over 21,000 events have been identified mostly within 0.3 AU during which the spacecraft was in the encounter mode and thus had a better complete data coverage. The SFRs via the SPAN-Ion data are mostly within 0.2 AU, typically near each perihelion. They supplement the gaps where the SPC data with the flag "Only Good Quality" were unavailable. Events spreading out from 0.4 to 1 AU are mainly contributed by SolO and Helios spacecraft. The detected SFRs using SolO data contain records from 2021 April 22 to 2023 April 24, which arise in a wide range of distances from 0.293 to 1.015 AU. The two Helios spacecraft were at similar ranges of radial distances as the SolO. Thus, they are utilized to minimize the impact of data gaps that may conceal the overall distribution. The SFRs via these two Helios measurements have a total of over 8,000 records. The range of V_{SW} is very similar among the three groups of results. It shows that SFRs in this study spread in both the slow and fast-speed solar winds. Figure 1(b) presents histograms of average solar wind speed for each group of events. Since both PSP and SolO spacecraft were mostly in the slow solar wind streams at low latitude regions for the past orbits, V_{SW} in these three groups peaks at a small speed, i.e., 350 km s^{-1}.

The ranges of duration and scale sizes are also similar among the four sets of events. More specifically, as shown in Table 1, three sets of results have broad ranges of scale sizes from a few kilometers to 0.19 AU and duration from 10 s to 17 hrs. Among them, 99.88% of intervals are less than 6 hours long, which corresponds to the commonly defined SFR. Whereas, a negligible portion of 0.12%

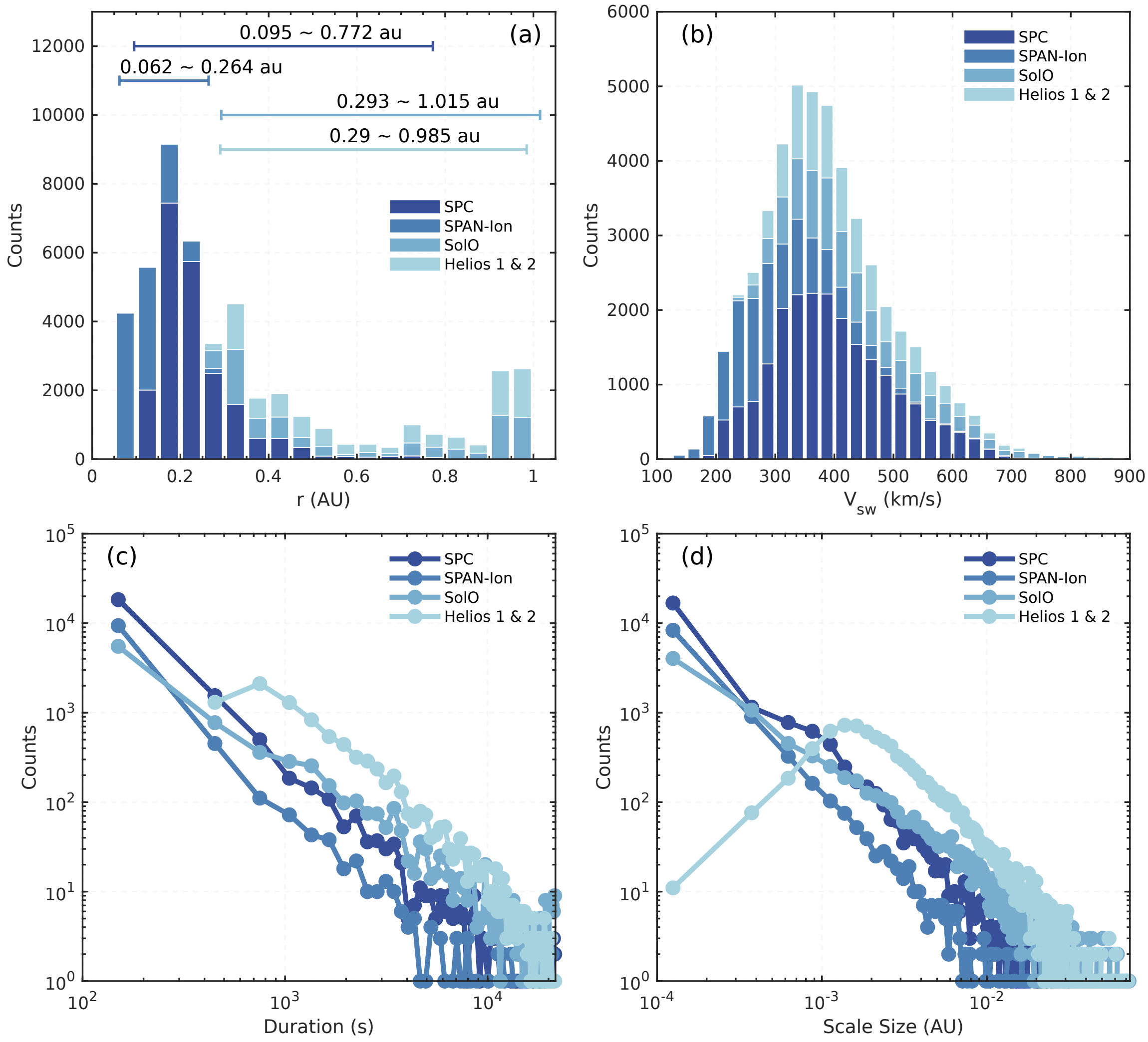

Figure 1. Distributions of the SFR properties: (a) radial distance of the occurrence, (b) average solar wind speed within SFR intervals, (c) duration, and (d) scale size. See the legends for the correspondence to the four datasets: PSP/SPC, PSP/SPAN-Ion, SolO, and Helios 1 & 2.

of events has duration longer than 6 hours, which is close to the scale size of the magnetic cloud. It should be understood that the results that the SFRs via Helios 1 & 2 have larger ranges of scale sizes and duration is due to a larger sampling interval or lower resolution of the Helios datasets. Therefore for a fixed set of search windows, the lower and upper limits of the range of duration become larger. Figure 1(c & d) display detailed distributions of SFR counts for duration and scale size. All four groups of events still seem to follow a power-law tendency, although the lower end of each distribution is affected by the data resolution. The limited sample sizes and uncertainty in the choices of the bin sizes prohibit us to provide more definitive conclusions about their distributions.

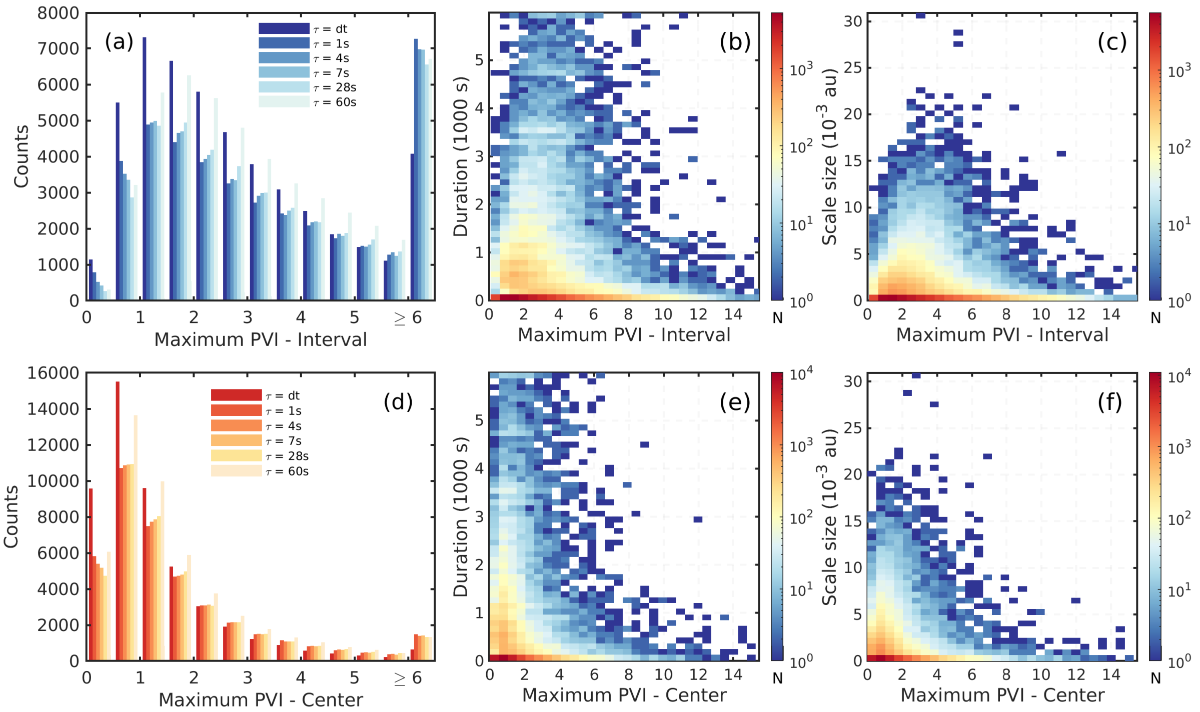

Figure 2. Distributions of SFR properties versus different maximum PVI values: (a & d) counts with different time lags τ (see the legend), (b & e) duration, and (c & f) scale sizes. The top row shows the distributions for the maximum PVI values within SFR intervals, whereas the bottom row shows those for the maximum PVI values near the turning point (usually the SFR center).

As aforementioned, with the increasing numbers of SFRs collected in our databases, it becomes an important question whether they are "contaminated" by current sheets. One way to signalize current sheets from the background solar wind is via the PVI index. As suggested by Greco et al. (2018); Chhiber et al. (2020), different values of PVI indices may hint at some special structures. For example, PVI values greater than 3 and 6 likely refer to non-Gaussian structures and current sheets, respectively. Notice that current sheets can often be detected at boundaries of SFRs, which often results in large PVI indices within SFR intervals. This usually does not affect the identification of an SFR structure (Pecora et al., 2019). Thus, we also examined PVI indices near the turning point, i.e., at the point with the extreme value of A (usually near the SFR center) as introduced in the Section 2. If the PVI indices are still large under such a circumstance, it is necessary to look further into whether they should be current sheet type or flux rope structures. In PVI calculations with $\tau = dt$, the time lag τ is designated as the time step dt of the time-series data for the GS-based detection, i.e., 1s, 4s, 7s, 28s, and 60s, respectively (depending on the original plasma data cadence). For a fixed τ, e.g., $\tau = 4$s, the magnetic field data is reprocessed to be 1s cadence for calculating the PVI values by Equation 3. Notice that SFRs via the two Helios datasets are taken into account in groups of $\tau = dt$ (60s for Helios datasets) and $\tau = 60$s only due to the resolution of the original data.

Figures 2 (a & d) show the counts of SFRs corresponding to the maximum PVI indices with different time lags for all events included in this study. Panel (a) represents the maximum PVI indices within SFR intervals, whereas panel (d) is those near the SFR center. When setting $\tau = dt$, there are more SFRs with smaller maximum PVI indices than those calculated with fixed time lags (e.g., $\tau =$1s), which is partially because SFRs via the two Helios data are not included in counts with $\tau =$1s. Without these two sets of events, 37% of SFRs are identified via the plasma data with the original resolution lower than 1s. Therefore, rapid changes in the magnetic field appearing with the original higher data resolution for the PSP and SolO might be smoothed after downsampling. On the other hand, counts of SFRs at larger maximum PVI indices with different time lags appear to be similar, which is likely due to slow changes in field rotations that become detectable with large time lags. The overall tendency is uniform with different τ. Around half of identified SFR intervals have maximum PVI indices greater than 3, which are consistent with the previous findings that SFRs have non-Gaussian features (Zheng & Hu, 2018). Less than 15% of events have those indices greater than 6, including those current sheet structures near the SFR boundaries. For the maximum PVI indices near the SFR center, these ratios become smaller, i.e., around 3%. Thus, only a small portion of events might be indistinguishable from current sheets with PVI > 6.

As aforementioned, the GS-based detection is constrained by the plasma data resolution that has lower cadences than those of the magnetic field. Therefore, we will still refer to PVI values with a time lag equal to the processed data resolution in the SFR detection, i.e., $\tau = dt$, for consistency. Figures 2 (b, c, e, f) present distributions of SFR duration and scale size at different maximum PVI indices within the interval and near the center respectively. SFRs with shorter durations and smaller scale sizes have wide ranges of maximum PVI indices and dominate the distributions in both groups. For the maximum PVI indices within SFR intervals, as the duration and scale size increase, such ranges become narrower and center around PVI ≈ 4. When using $\tau = 1$s, the center is around PVI ≈ 8 (not shown as they do not include Helios results). Given a limited sample size, these tendencies may indicate that relatively larger or longer SFRs have more current sheets at boundaries or areas other than the center. For the maximum PVI indices near the SFR center, they have similar narrowing tendencies as increasing scales but tend to be around smaller maximum PVI indices, i.e., around 2 (maximum PVI ≈ 4 for $\tau =$1s). These PVI indices refer to non-current sheet types. It is expected that relatively longer or larger SFRs often have gradual bipolar field rotations, while current sheets usually correspond to more abrupt changes.

Table 2. Overview of selected SFRs with large PVI values.

Case No.	Time period (UT)	Radial distances (AU)	Scale size (AU)	PVI_{max}	$PVI_{turning}$
1	2020 June 8, 14:42:50-15:16:47	0.14	0.001	9.46	6.078
2	2022 September 23, 01:02:48-06:01:28	0.526	0.032	5.537	5.389
3	2022 October 21, 17:50:48-18:19:16	0.759	0.004	7.149	7.149

With $\tau = dt$, 8.27% of events possess the maximum PVI indices > 3 near the SFR center. Considering the large number of events, the batch mode of the GS reconstruction with the default settings is adopted for a quick run to generate the cross-sectional maps. Among 2,591 events showing satisfactory reconstruction results and thus without the need for further manual adjustments, we found that these SFRs can be categorized into three major types. (1) The spacecraft crosses near the center(s) of one or more SFRs where the transverse magnetic field directions have nearly opposite directions. (2) The spacecraft crosses the SFR(s) but not through the center, and the transverse magnetic field directions have abrupt changes but not complete reversals. (3) The spacecraft crosses the open magnetic field lines, which exhibit an "X" shape with opposite field directions from one side to the other. 85% of the aforementioned events are found to be either the first or second type. Again, SFRs with shorter duration and smaller scale sizes dominate in all three groups of events, which may conceal the intrinsic dependencies on the PVI indices (if any). In the following, we select three representative cases with relatively large PVI indices in each aforementioned category. The overview of these cases is listed in Table 2, including the case sequential number, time period, radial distance, scale size, the maximum PVI index within the whole interval, and that near the center. Two of three cases own large PVI indices within the event interval and near the SFR center. The second case has a PVI index of around 5 and is regarded as a marginal case regarding the above PVI criteria since it does show an interesting signature.

3.1 Case No.1: Current Sheets Inside an SFR

Figure 3 presents the first case in Table 2, i.e., for an SFR interval on 2020 June 8, from 14:42:50 to 15:16:47 UT. During this time period, the PSP spacecraft was at around 0.14 AU, which is a day behind its fifth perihelion. Panels (a & c) show the $P_t(A)$ curves that are used to reconstruct this SFR structure and its corresponding cross sectional map. In panel (a), the blue circles and red stars describe $P_t(A)$ values from the left boundary on panel (c) to the turning point (near the white dot), and then from it to the right boundary. The two sets of data points consist of a double-folding pattern of $P_t(A)$, i.e., the two sets of symbols overlapping and a single fitting function can be obtained as illustrated by the black

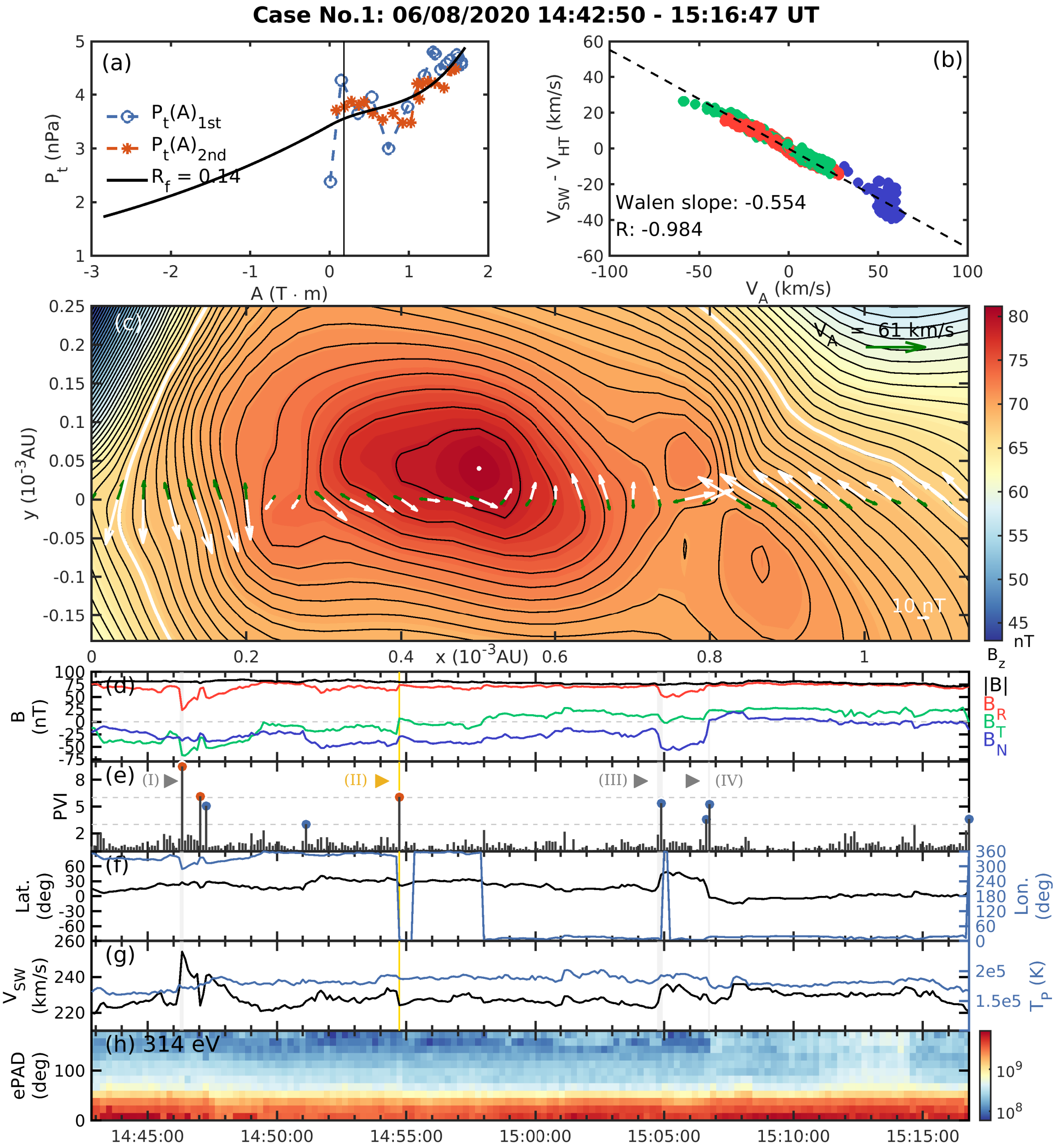

Figure 3. Results of the GS-type reconstruction and time-series plot for Case No.1: 2020 June 8, 14:42:50 to 15:16:47 UT. Panels (a-c) show the $P_t(A)$ data points and the fitting curve (black), the Walén relation, and the cross sectional map with the axis orientation z=[0.94, 0, -0.34] in RTN coordinates respetively. Panels (d-h) are the time-series plot of the same interval, which includes the magnetic field components in RTN coordinates and its magnitude, PVI index, latitudinal and longitudinal angles of the magnetic field, solar wind speed V_{SW} and proton temperature T_p, and the ePAD at 314 eV respectively. Yellow and gray shaded areas (denoted by triangles and roman numbers) mark selected subintervals where large PVI indices occur. The yellow color here is to point out that this jump is close to the flux rope center.

curve, which is a core feature of the GS reconstruction technique. On the cross sectional map, the black contours indicate the transverse magnetic field $\mathbf{B}_t$ in the co-moving frame, which forms a closed field line region in the center. The background colored areas represent the axial field B_z, which depicts a unipolar feature coinciding with the central contour lines. These two features thus confirm a flux rope structure with right-handed chirality as indicated by the white arrows along $y = 0$. The turning point (time) of this event is at 2020 June 8, 14:56:22 UT, which is close to the maximum B_z (white dot). Along the spacecraft path (at $y = 0$), the transverse remaining flow (green arrows) are mostly anti-aligned with the $\mathbf{B}_t$ vectors as drawn and are generally a fraction of the average Alfvén speed as shown in magnitude. This is also demonstrated in panel (b), which shows the Walén relation between the remaining flow and the Alfvén velocity V_A. The linear regression slope is -0.554, thus indicating a modest Alfvénic structure.

The bottom panels (d-h) of Figure 3 show the corresponding time-series variations of this SFR interval containing the magnetic field in the RTN coordinates and its magnitude, the values of PVI indices, the latitude and longitude angles of the magnetic field, solar wind speed V_{SW} and proton temperature T_p, and the electron pitch angle distribution (ePAD) at 314 eV. To be consistent with the detection dataset, the 7s averaged data are adopted due to the resolution of the plasma data. Shaded areas represent selected intervals with large PVI indices and are thus examined further to see if each is a reconnection exhaust. During the whole SFR interval, the field component B_T gradually changes from being negative to positive building a bipolar rotation, while B_R and B_N mostly remain positive and negative respectively. The unidirectional electron strahls are throughout the whole event interval (Figure 3h). Panel (e) shows the PVI indices at each data point, with the threshold values of 3 and 6 denoted by the horizontal dashed lines. At a glance, there are four regions with abruptly large PVI indices, which are around (I) 14:46, (II) 14:54, (III) 15:05, and (IV) 15:06 UT. Note that we would first name these structures "jumps" to describe those sudden changes in the field components, and discuss the confirmation of the current sheet structure later. Among them, the second jump (No.II, marked by a yellow area) is close to the SFR center, while the other three are near the SFR boundaries. The PVI index for this jump is 6.078 as listed in Table 2. It is accompanied by a small change in latitude, i.e., around 20 degrees. The shear angle of the total magnetic field between two edges of the yellow area is 40°. Both V_{sw} and T_p have dips simultaneously at the two edges.

Since the second significantly large PVI jump (interval No.II) is close to the SFR center, it raises the same question as aforementioned at the beginning of this subsection: is it a flux rope or a current sheet? Figure 4 presents a zoomed-in view of each interval around those jumps. Panels (a-d) correspond to the Roman numbers (I-IV) in Figure 3. The boundaries of each jump are visually identified, which are chosen at locations around the relatively steady magnetic field before and after the sudden jumps. The first

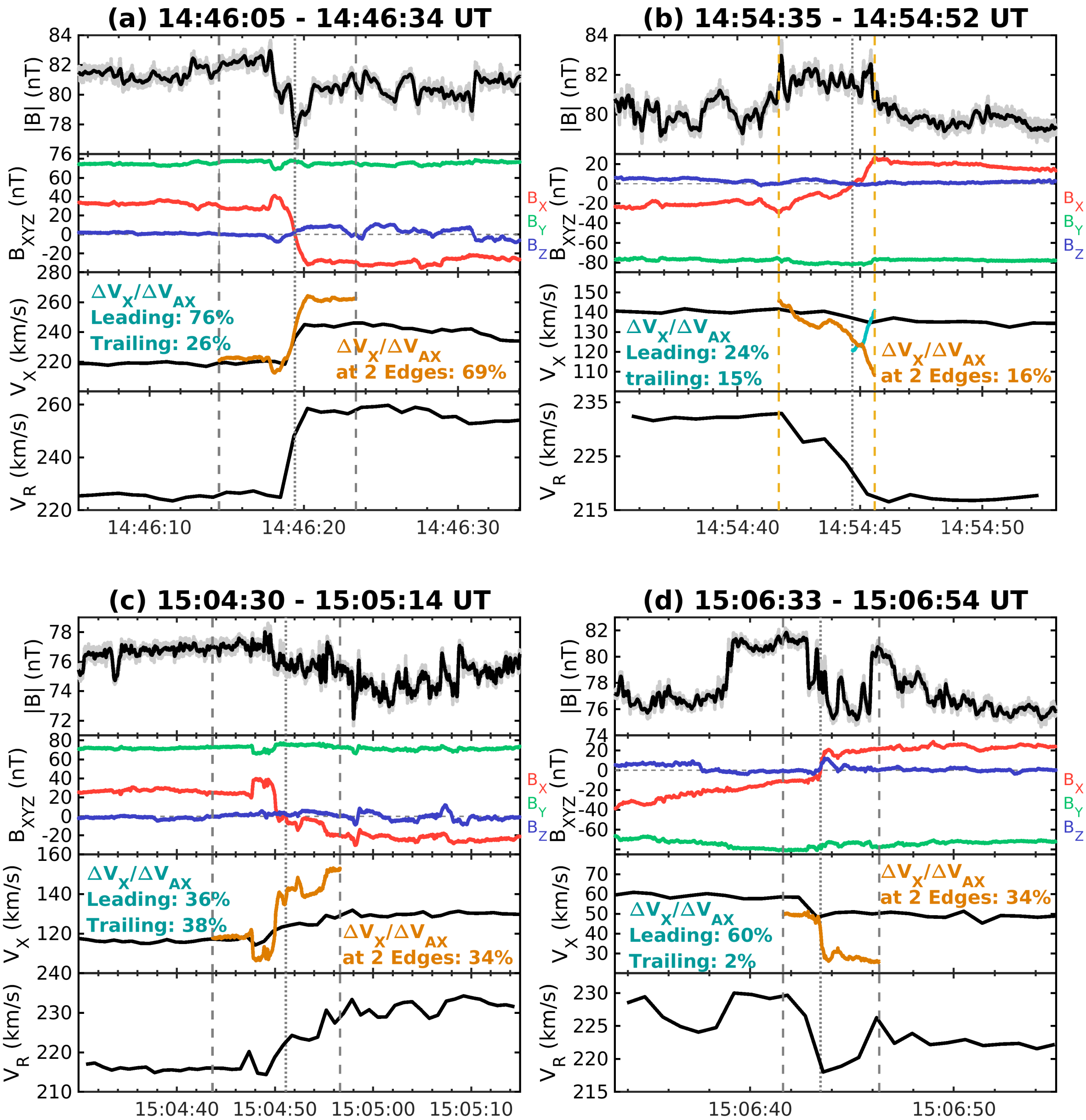

Figure 4. Zoomed-in time-series plots of the yellow and gray shaded areas (I-IV) in Figure 3 on June 8, 2020, which are marked by (a-d) respectively. For each subfigure, panels from the top to bottom are the field magnitude $|B|$ with the original data resolution (gray line) and its moving average (black line), the magnetic field in the principal XYZ coordinates, V_X and the predicted velocity (cyan and orange lines), and the radial solar wind speed V_R. Boundaries of jumps are denoted by two vertical dashed lines. Again, the yellow color here points out that this interval is close to the flux rope center. Three ratios of $\Delta V_X/\Delta V_{AX}$ are calculated based on the assumption of a bifurcate current sheet (cyan) and a single current sheet (orange) respectively. See texts for more details.

panel of each interval shows the magnitude of the magnetic field with its original data resolution (gray line) and the running average (black line) for presenting purposes. The second panel shows the magnetic field in the hybrid current sheet coordinate system, also known as the LMN coordinate (Gosling & Phan, 2013). To separate it from the RTN coordinates, we denote this coordinate system by XYZ. Following (Gosling & Phan, 2013), the Z component is obtained by $B_l \times B_r/|B_l \times B_r|$, where the subscripts "l" and "r" indicate the magnetic field at the current sheet left and right boundaries (two dashed lines in Figure 4). The Y component is calculated by crossing Z and the maximum variance direction via the minimum variance analysis of the magnetic field (MVAB, Paschmann and Daly (1998)). Finally, the X component is completed by $Y \times Z$. On the second panel, the component B_X along the direction tangential to the current sheet shows a stair-like variation, whereas the component B_Z is around the zero line as it corresponds to the normal component. The third panel shows the solar wind velocity denoted by black line and the predicted velocities in X-direction marked by cyan and orange lines. The cyan lines represent the predicted velocity based on the assumption of a bifurcate current sheet, which usually consists of two RDs at the two edges and thus obtained via the two separate Walén tests (Phan et al., 2020). The orange line is obtained under the assumption that there is only one current sheet or discontinuity corresponding to the dotted line in the middle. We will present the best matched predicted velocity lines only for the rest of the cases. In particular, we follow Phan et al. (2020) to label the ratio $\Delta V_X/\Delta V_{AX}$. Notice that three ratios are marked on the third panel. Those denoted by "leading" and "trailing" indicate changes across two edges of the presumably "bifurcate" current sheet, i.e., from inflow to outflow regions. They are derived from the Walén relation $V_{X2} - V_{X1} \sim \pm(B_{X2} - B_{X1})/(\mu_0\rho_1)^{1/2}$. Here, the subscript "1" represents the inflow region, which corresponds to the average before the leading edge (left vertical dashed line) or the average after the trailing edge (right vertical dashed line), respectively. The subscript "2" corresponds to the current sheet center (vertical dotted line). The third ratio indicates the differences of V_X and V_{AX} between the two edges. Therefore, it can represent the Alfvénicity of a single current sheet interval to some extent.

Notably, in Figure 4(b), the field magnitude $|B|$ in interval No.II increases slightly when approaching the center of the current sheet. The reconnection exhaust with a bifurcate current sheet can usually be seen if the components B_X and V_X correlate positively at one edge and possess anti-correlation at the other, or vice versa. However, the V_X in this interval seems to not correlate with the B_X as $\Delta V_X/\Delta V_{AX}$ for the whole area is only 16%. Changes in V_X across the leading and trailing edges are only 24% and 15% of ΔV_{AX}. Therefore, without clear Alfvénic proton jets in the outflow region, it is unlikely to be a bifurcated current sheet associated with a reconnection exhaust. Instead, it could be a single RD as neither significantly depressed field strength nor enhanced T_p is observed at this current sheet.

As aforementioned, there are additional time periods also corresponding to sudden PVI index jumps, which are marked by the gray areas (I), (III), and (IV) in Figure 3. Based on the cross-sectional map in Figure 3(c), they occur near the boundaries of a flux rope or the intersection between the main structure and sub-structure. As shown on the Figure 3(e), the first jump has a PVI index above 8, whereas the last two are slightly below 6 (the upper horizontal dashed line). Moreover, they are accompanied by 20 to 30 degrees change in either latitude or longitude angles of the magnetic field. The first and third jumps also have clear increases in the solar wind speed, while the last one seems to be similar to the one near the SFR center, i.e., both V_{SW} and T_p drop.

Figure 4(a, c, & d) also show the zoomed-in views of these three areas (corresponding to I, III, & IV in Figure 3). The second panel of each interval shows a clear and abrupt monotonic rotation of B_X from one sign to the opposite sign, which hints at the current sheet structures. Magnitudes of the magnetic field in the first and last intervals dip around the center of current sheets (vertical dotted line) where the B_X crosses the zero-line. Shear angles of the magnetic field between two vertical dashed lines are 42°, 34°, and 23°, respectively. Although with the lower resolution of V_X, the entire intervals (between two vertical dashed lines) in Figure 4(a, c, &d) seem to have V_X anti-correlated with B_X. Notice that the last two intervals (areas III & IV) are only separated by 1 minute. As shown in Figure 4(d), the two current sheets can be regarded as boundaries to enclose a substructure. In fact, the extended interval from 15:04:30 to 15:06:54 UT also has B_X anti-correlated with V_X (not shown). Thus, none of these three jumps have clear associations with reconnection exhausts, i.e., complying with the classification as reconnecting current sheets.

In summary, this case represents a situation in which an SFR interval contains one or more current sheets, which are crossed by the spacecraft and thus result in large PVI values. Although the maximum PVI index exceeds 8 within this SFR interval, it occurs near the boundary where the magnetic field changes direction more significantly than other points. All four current sheets with relatively large PVI values exceeding 5 are non-reconnecting type, which lacks the plasma jet in the outflow regions. The ratios between ΔV_X and ΔV_{AX} at two edges of all current sheets in Figure 4, i.e., 69%, 16%, 34%, and 34%, illustrate that they could be one single RD, instead of a reconnection exhaust bounded by two RDs. Moreover, since unidirectional electron strahls are throughout the whole interval, these current sheet structures are more possibly be boundaries of a magnetic switchback (Kasper et al., 2019). This switchback is quite weak and does not appear to have strong reversals of the magnetic field in the time-series plot. Although the one near the SFR center also has a large PVI index, it only has a small rotation of the magnetic field direction. This small change is embedded in a background with a more general bipolar rotation where one field component changes the sign over the SFR interval. Such a co-existence of the SFR and large PVI index is also similar to the O-point type in Pecora et al. (2019), where the current core is near the SFR center.

3.2 Case No.2: SFR With Arbitrary Kinks

Figure 5 shows the case No.2 in Table 2, whose interval starts from 2022 September 23, 01:02:48 UT and ends at 06:01:28 UT. This SFR is longer in duration as compared with the other two cases. The scale size, as represented by the range of the x-axis of Figure 5(c), is about 0.032 AU. As usual, panel (a) also shows a clear double-folding pattern of $P_t(A)$. This SFR is left-handed and possesses a modest level of Alfvénicity, i.e., the Walén test slope is 0.405. On time-series plots of the whole interval, one can see that V_{SW} near the two boundaries of this SFR have different values, whose minimum and maximum are 276 and 321 km s^{-1} respectively. Thus, the trailing region of this SFR might be in a faster stream. Moreover, there are clear bidirectional electron strahls, especially for the time period after 03:00 UT. This could hint that the corresponding magnetic field lines have both ends rooted at the Sun. In other words, this SFR could be initially formed in the low corona, ejected into the solar wind, and finally traversed by the PSP at 0.526 AU.

Figure 5(e) presents several jumps in the magnetic field measurements including two significant ones, i.e., areas as marked by Roman numbers (I) and (II), whose PVI indices are close to 6 (the top horizontal dashed line). The jump near the SFR center, as marked by the yellow area and roman number (II), is accompanied by a sudden dip in the latitude and a narrow peak in the V_{SW}. The corresponding shear angle for this jump is 53°. This jump is within a dip-like region as exhibited in Figure 5(d). Figure 6(b) displays the corresponding time period for area (II) in detail. Again, unlike the traditional current sheet, the magnitude of the magnetic field during this period is on the increase phase. The general shape of V_X seems to change similarly to that in B_X, which is somewhat hidden because of the 28s cadence plasma data at this radial distance. Three ratios of $\Delta V_X/\Delta V_{AX}$, i.e., 248% when crossing the leading edge, 60% when crossing the trailing edge, and 73% at two edges, show strong Alfvénic correlations. Combining the variations of the B_R in Figure 5d, which change from below zero-line to positive and then become negative again after crossing the current sheet center (the dotted line in Figure 6b), this interval could be a part of the magnetic switchback structure within an SFR interval (Chen et al., 2021). It can also be an arbitrary kink since the spacecraft traverses the perimeter of this SFR instead of the center, contrary to Figure 3(c).

As mentioned above, the PVI indices within this interval have two significant jumps close to 6. Figure 6 also displays the first jump out of the above two and the one selected from the other 10 jumps

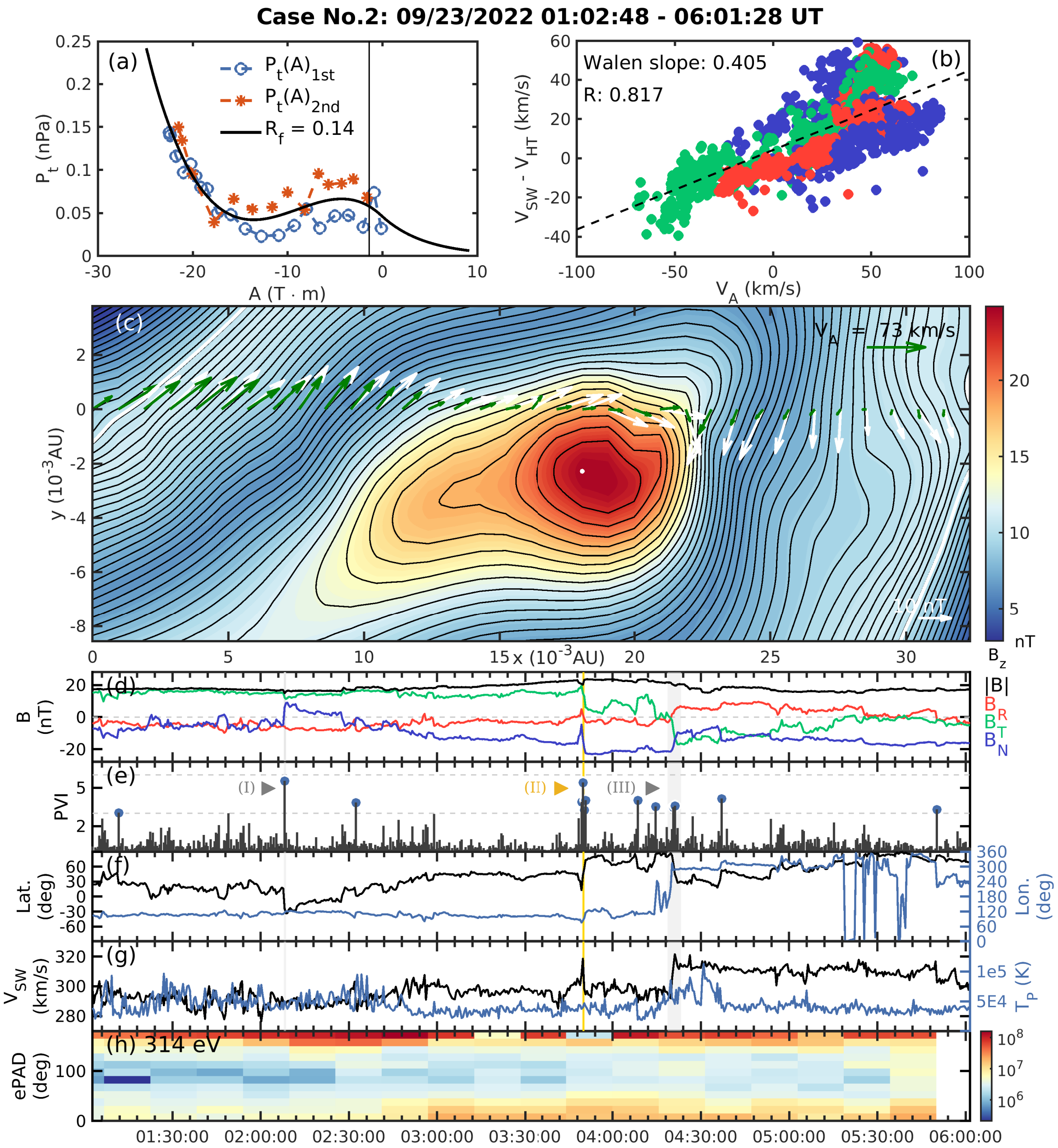

Figure 5. Results of the GS-type reconstruction and time-series plot for Case No.2: 2022 September 23, 01:02:48 to 06:01:28 UT. The flux rope axis is z=[0.49, 0.41, -0.77] in RTN coordinates. The format follows that of Figure 3.

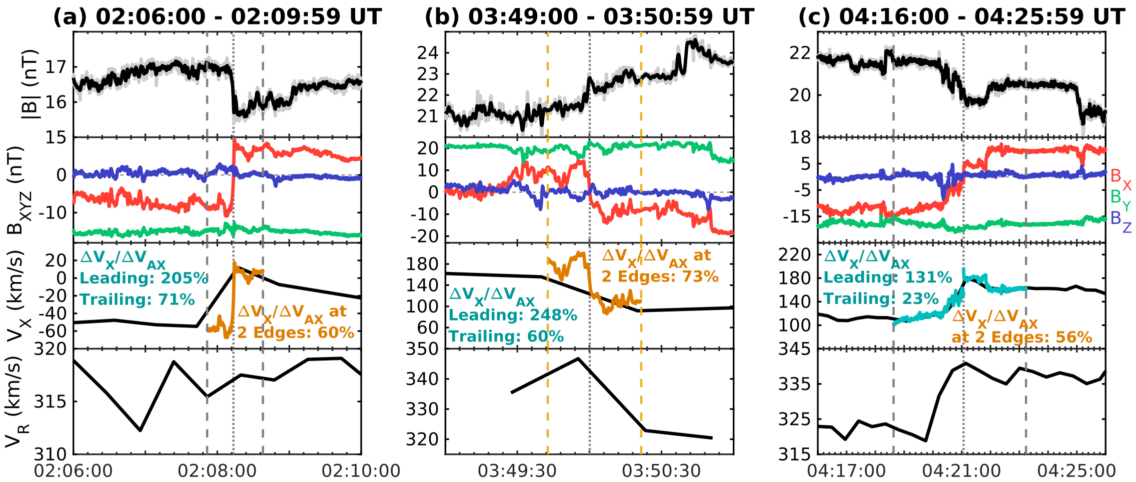

Figure 6. Zoomed-in time-series plots of yellow and gray shaded areas (I-III) in Figure 5. The format follows that of Figure 4.

that have PVI indices exceeding 3, as shown in subfigures (a & c). The interval (a), although affected by the resolution of the plasma data, reveals a positive correlation between B_X and V_X. The leading edge has a strong Walén relation with a ratio to be over 100%, which can also be seen in Figure 5(a). The time period of this jump corresponds to the left top region on the cross-sectional map. The remaining flow vectors are quite large compared with the Alfvén speed. Also, they appear to be aligned with the transverse field $\mathbf{B}_t$. Thus, the Alfvénicity around such a region is very high indeed. The panel (c) shows a time period where the PSP traversed at the boundary of the main SFR structure. The signatures in V_X hint at the reconnection exhaust. At the leading edge, V_X and B_X form the Alfvénic correlation with the ratio to be >100 %, whereas the trailing edge has clear anti-correlation with B_X as shown by the cyan line as well.

In summary, this case could be a scenario in which an SFR is generated after the magnetic reconnection at a relatively large current sheet, where the main structure is in the outflow region and the left top region on the cross-sectional map has very large remaining flow vectors compared with the corresponding Alfvén speed in this interval. The aforementioned current sheet together with the SFR are not fully traversed by the spacecraft. Thus, the expected nearly symmetric outflow on the other side of the SFR is uncertain, likely due to the spacecraft path that did not traverse along the normal direction of the current sheet. One boundary of the reconnection exhaust might correspond to that of this SFR, while the other boundary is possibly out of the range of the cross-section map. Again, large PVI indices still exist at the boundaries of the SFR, which hint at small current sheets. Considering that the counterstreaming electrons exist in the whole interval as an indicator of closed field-line connectivity for a magnetic flux rope structure, it could be an arbitrary kink as the spacecraft did not cross the center the this SFR structure.

3.3 Case No.3: False Identification of an SFR

Figure 7 shows the case No.3 in Table 2, which starts from 2022 October 21, 17:50:48 UT to 18:19:46 UT. Unlike the other two cases, the GS reconstruction result shows a clear current sheet structure. The duration of the interval is only 20 minutes. Panel (c) depicts the magnetic field lines that change polarities clearly along the spacecraft path. Although the remaining flow vectors also change to the opposite direction, there are some deviations from the $\mathbf{B}_t$ vectors. Therefore, the Alfvénicity of this interval is weak, which was also indicated by the panel (b), i.e., the corresponding Walén test slope is 0.3. The most uncertain signature is the double-folding pattern of $P_t(A)$ although it is understood that it is not a necessary and sufficient condition for the existence of a flux rope structure. Panel (a) seems very similar to those of the other two cases, which could be the major reason for this event to be falsely identified as an SFR. In the time-series plot, the magnetic field has clear changes with a shear angle of 97°. All three components have the apparent bipolar rotations, which is supposed to hint at flux rope structures. However, these rotations are through step-wise jumps, or in other words, rapid change of signs. Such changes are also reflected by a significant value of the PVI index exceeding 6 and around 60 degrees change in longitude (around 30 degrees in latitude) in the middle of the interval. Notice that these signatures all occur near the center of this interval. The last panel of Figure 7 shows a clear ePAD signature, indicating that the corresponding magnetic field lines change connectivity, although the timing is a little off due to low data resolution. In addition, the cross-section map shown in Figure 7(c) is similar to the 2D configuration of a bifurcate current sheet reconstructed in Teh et al. (2009).

The zoomed-in view in Figure 8 further shows what happened near the "SFR" center. The strength of the magnetic field drops, and the B_X component shifts the sign abruptly. The proton jet is very weak compared with the predicted velocity since the spacecraft traversed the inflow region mostly and nearly crossed the X line as shown by Figure 7(c). Therefore, it is unlikely to record a strong outflow region (if any).

In summary, based on the GS reconstruction result, this event should be a current sheet, which was mistakenly identified as an SFR. It has a clear dip in the magnitude of the magnetic field, a significantly large PVI index, and the corresponding discontinuous variations of electron strahls. The expected jet is very weak due to the spacecraft path that did not cross the outflow region.

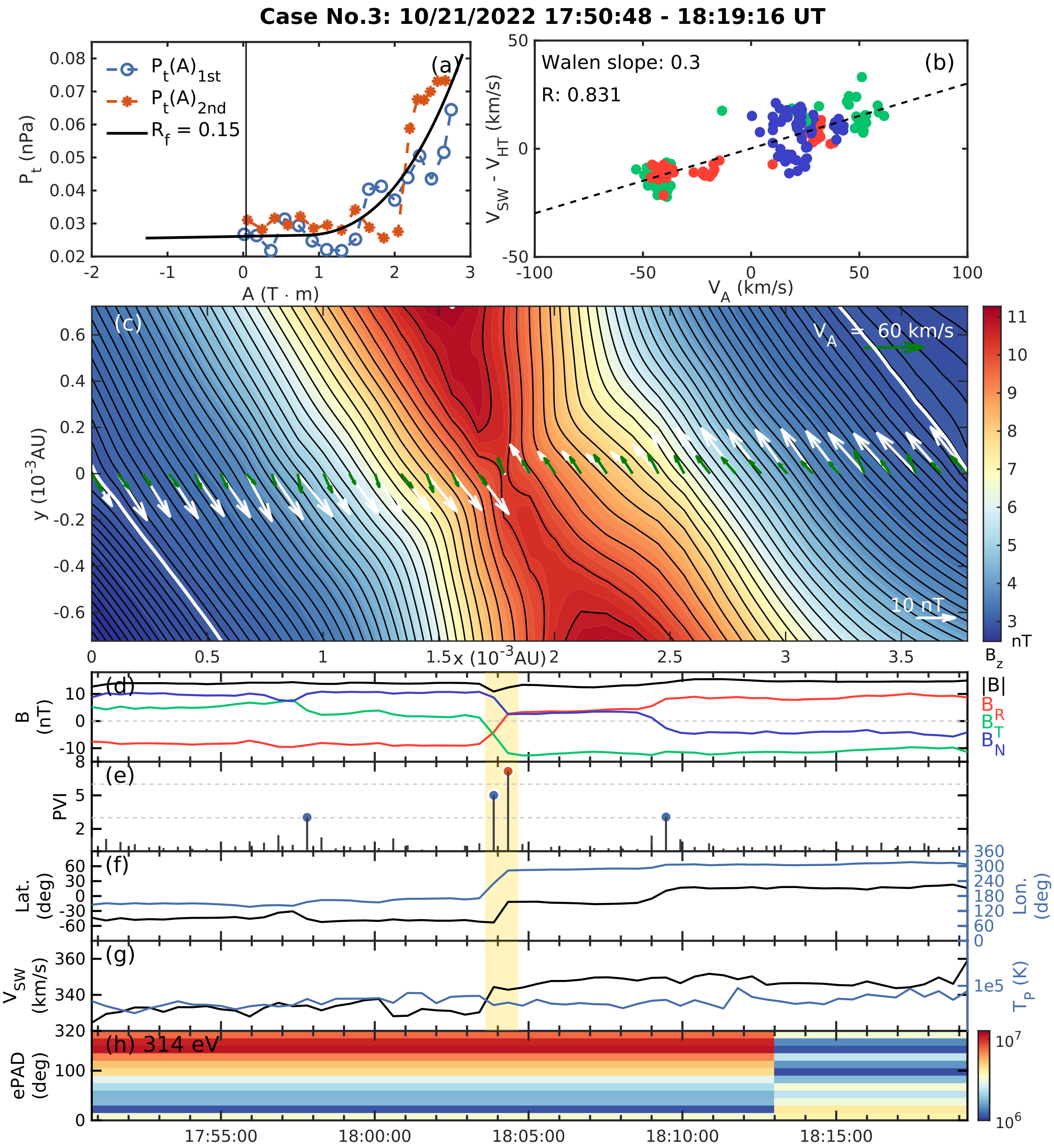

Figure 7. Results of the GS-type reconstruction and time-series plot for Case No.3: 2022 October 21, 17:50:48 to 18:19:16 UT. The flux rope axis is z=[-0.13, -0.75, 0.64] in RTN coordinates. The format follows that of Figure 3.

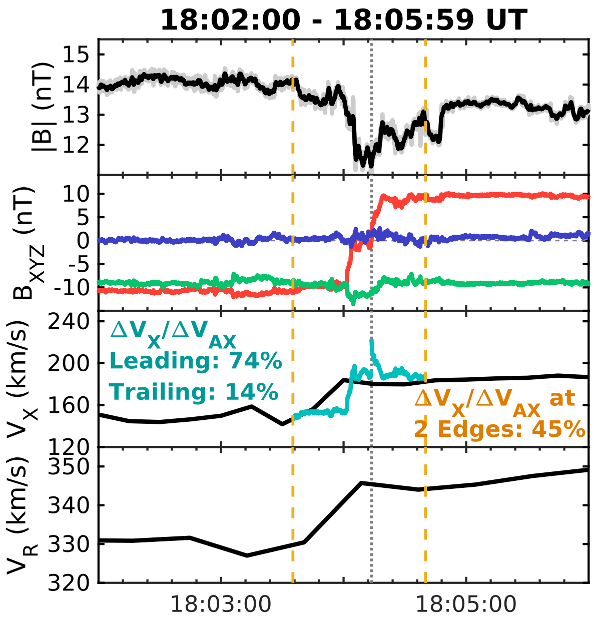

Figure 8. Zoomed-in time-series plots of the single yellow shaded area in Figure 7. The format follows that of Figure 4(a).

4 Summary and Discussion

We report the recent GS-based detection results obtained from four in-situ spacecraft datasets. They include the PSP data covering fifteen orbits, the SolO data from April 2021 to April 2023, and data from the full mission periods of the two Helios spacecraft. We present the overview of the identified SFRs, which occur almost across all heliocentric distances from 0.062 to 1.015 AU. In total, 48,736 SFRs are identified from the four spacecraft datasets with variable cadences. They have duration and scale sizes range from 10 s to 17 hrs and 1.97×10^{-6} to 0.19 AU, respectively. They also exist in a wide range of solar wind speeds and tend to be more frequently associated with relatively slow solar wind speeds around 350 km s^{-1}, given the aforementioned in-situ spacecraft observations.

Among these SFRs, we examine those containing large PVI indices as they may hint that the magnetic field rotation was not always an indicator for an SFR, an intrinsic fact that was known, but not well studied. The resulting statistics demonstrate that less than 15% of SFRs have the maximum PVI indices larger than 6, a threshold for current sheet identification. Events with PVIs exceeding this value mostly possess the corresponding maximum PVI indices near boundary areas. When further examining those indices near the SFR center, only around 3% of events are possibly false identification of SFRs with the corresponding PVI indices exceeding 6. In addition, SFRs with shorter durations and smaller scale sizes appear to have wide ranges of maximum PVI indices including those near the

SFR center. Based on the limited sample size, as scales increase, they may have more current sheets at boundaries, while the field rotations near the SFR centers tend to be gradual changes rather than rapid characteristics of current sheets. When considering a more relaxed threshold value of the PVI index, around half of SFR intervals have the maximum PVI values greater than 3, which indicates that they possess non-Gaussian features. Also, the co-existence of SFRs and current sheets again hints at the possible MHD turbulence generation mechanism for these structures at all distances from near the Sun to 1 au.

For SFRs that might co-exist with or be indistinguishable from current sheets, we find three categories of events via the batch mode of the GS reconstruction. They do not appear to have any obvious dependencies on the PVI indices given limited sample sizes. A representative type of event in each category is selected and analyzed, which represents the situations that (1) an SFR with current sheets near the center and at boundaries, (2) an SFR with arbitrary kinks and is embedded in the outflow region, and (3) a current sheet that is falsely identified as an SFR. Under the first circumstance, both the SFR main structure and current sheets are crossed by the spacecraft. Four subintervals around the calculated PVI jumps are investigated in detail. Three jumps occur near the flux rope boundaries or between the main flux rope structure and the sub-structure. Only one PVI jump is near the flux rope center. This likely corresponds to the "O-type" event classified by Pecora et al. (2019), where the current sheet discontinuity is an "O" point rather than a "sheet" like structure. The unidirectional electron strahls are throughout the whole SFR interval, and all four jump regions contain modest to high Alfvénic correlation without a clear signature of proton jets. Thus, for this case, we conclude that a single one-side RD exists, while the reconnection exhaust bounded by two RDs is not seen based on the analysis results of Walén relations for each subinterval. The large PVI index near the flux rope center could also be a weak spike boundary or a "current sheet" embedded within the O point. The magnetic field rotation is small around this jump, which is in the background of a more gradual bipolar rotation. Notice that although this case presents a main SFR and the substructure, a single SFR crossed by the spacecraft near the center is also categorized to this type since the large PVI value near the SFR center is likely due to the current core as discussed above (see also Pecora et al. (2019)).

The second case possibly depicts a flux rope embedded in an outflow region of the magnetic reconnection exhaust. Again, it has gradually varying bipolar rotations of the magnetic field. There are noticeable counterstreaming electrons, which hints at a closed field-line topology with possible field-line connectivity to the Sun. The PVI jump on one side of the outflow region corresponds to a strong Walén relation where $\Delta V_X/\Delta V_{AX}$ is 60%. This is also evident between the remaining flow and the Alfvén velocities on the SFR cross-section map. The other side, however, does not contain such strong characteristics due to the spacecraft path deviating from the outflow region. The other PVI jump takes place near the SFR center, which also has a large $\Delta V_X/\Delta V_{AX}$ ratio between the two edges of the jump, i.e., 73%. Again, no proton jet shows up. Considering that the spacecraft only traverses the SFR near the perimeter, this could be an arbitrary kink instead of a current sheet. This type of events can also have multiple SFRs with possible current sheets in between while the spacecraft only traverses the periphery part of the whole structure.

The third case represents the falsely identified SFR. It has almost the same characteristics as an SFR, such as the double-folding pattern of $P_t(A)$, and bipolar rotations of the magnetic field, etc. The significant PVI index and variations of electron strahls indicate a current sheet crossing instead of encountering an SFR. There could be a reconnection exhaust associated with this current sheet. However, since the spacecraft may have only traversed the inflow regions, the proton jet is very weak.

The above three types of events could correspond to a scenario with each being enclosed by a large-scale current sheet, i.e., the HCS, similar to the scenarios of multiple islands/flux ropes at the Earth's magnetopause current sheet (Hasegawa et al., 2006, 2010). For example, we notice that a 3-hr HCS crossing in the PSP encounter No.14 has been reported in Phan et al. (2024) with signatures of multiple flux ropes embedded. These events are rare and generally embody significant uncertainties due to limited single-point measurements. We will pursue detailed analysis in future work.

One should also note that to distinguish whether there is a current sheet inside an SFR (Gosling & Phan, 2013), a current sheet between two SFRs or flux tubes (Fargette et al., 2021), or a mistakenly recognized SFR event, the most definitive way to separate SFRs from current sheets and vice versa is still via the multi-point spacecraft measurements. In addition, one can also address whether an SFR could have moderate to high Alfvénicity and its implications with our approach. Another fundamental open question is regarding the sources generating these SFRs, which could benefit from a combination of in-situ measurements and remote sensing observations. Wood et al. (2023) presented six small CME flux ropes by combining Wide-field Imager for Solar Probe (WISPR) images and time-series data from FIELDS and SWEAP. N. Huang et al. (2023) recently compared SFR occurrences with mini-filaments at the Sun. They found that the occurrence rate of mini-filaments is far more than that of SFRs. Although it is possible that mini-filaments could evolve to be several different structures after detaching from the Sun, the observation of those events is over the whole solar surface, while the in-situ observation is mostly limited in space and time, i.e., often only in the low latitude regions at one point at a time. Therefore, re-examining these properties using up-to-date new and future missions, such as SolO, HelioSwarm

(Spence, 2019; Klein et al., 2023), etc., as well as combining remote sensing data will be essential to our future work.

5 Open Research

The PSP and SolO data in this study are downloaded from the NASA CDAWeb (https://cdaweb.gsfc.nasa.gov/index.html/), and the Helios 1 & 2 data are from https://helios-data.ssl.berkeley.edu/data/. The GS-based detection and GS-type reconstruction results are obtained using the PyGS package, which is published at the Python in Heliospheric Community website at https://heliopython.org/ and our GitHub at https://github.com/PyGSDR/PyGS. The SFR event lists are available on the flux rope database at http://www.fluxrope.info/.

Acknowledgments

We would like to thank Dr. Jia Huang and Dr. Lingling Zhao for helpful suggestions and discussions. Y.C. and Q.H. acknowledge NASA grants 80NSSC21K0003, 80NSSC21K1763, 80NSSC21K1319, and NSF grant AGS-2229065 for support. This work was made possible in part by a grant of high performance computing resources and technical support from the Alabama Supercomputer Authority.

References

Bale, S., Goetz, K., Harvey, P., Turin, P., Bonnell, J., De Wit, T. D., ... others (2016). The fields instrument suite for solar probe plus. *SSRv*, *204*(1-4), 49–82. Retrieved from https://doi.org/10.1007/s11214-016-0244-5 doi: 10.1007/s11214-016-0244-5

Borovsky, J. E. (2008, August). Flux tube texture of the solar wind: Strands of the magnetic carpet at 1 AU? *Journal of Geophysical Research (Space Physics)*, *113*, A08110. doi: 10.1029/2007JA012684

Case, A. W., Kasper, J. C., Stevens, M. L., Korreck, K. E., Paulson, K., Daigneau, P., ... others (2020). The solar probe cup on the parker solar probe. *ApJS*, *246*(2), 43. Retrieved from https://doi.org/10.3847/1538-4365/ab5a7b doi: 10.3847/1538-4365/ab5a7b

Chen, Y., & Hu, Q. (2020, may). Effects of radial distances on small-scale magnetic flux ropes in the solar wind. *ApJ*, *894*(1), 25. Retrieved from https://doi.org/10.3847/1538-4357/ab8294 doi: 10.3847/1538-4357/ab8294

Chen, Y., & Hu, Q. (2022, jan). Small-scale magnetic flux ropes and their properties based on in situ measurements from the parker solar probe. *ApJ*, *924*(2), 43. Retrieved from https://doi.org/10.3847/1538-4357/ac3487 doi: 10.3847/1538-4357/ac3487

Chen, Y., Hu, Q., Allen, R. C., & Jian, L. K. (2023, jan). Small-scale magnetic flux ropes in stream interaction regions from parker solar probe and wind spacecraft observations. *The Astrophysical Journal*, *943*(1), 33. Retrieved from https://dx.doi.org/10.3847/1538-4357/aca894 doi: 10.3847/1538-4357/aca894

Chen, Y., Hu, Q., & le Roux, J. A. (2019, aug). Analysis of small-scale magnetic flux ropes covering the whole ulysses mission. *ApJ*, *881*(1), 58. Retrieved from https://doi.org/10.3847/1538-4357/ab2ccf doi: 10.3847/1538-4357/ab2ccf

Chen, Y., Hu, Q., Zhao, L., Kasper, J. C., & Huang, J. (2021, jun). Small-scale magnetic flux ropes with field-aligned flows via the PSP in situ observations. *ApJ*, *914*(2), 108. Retrieved from https://doi.org/10.3847/1538-4357/abfd30 doi: 10.3847/1538-4357/abfd30

Chhiber, R., Goldstein, M. L., Maruca, B. A., Chasapis, A., Matthaeus, W. H., Ruffolo, D., . . . Raouafi, N. (2020, feb). Clustering of intermittent magnetic and flow structures near parker solar probe's first perihelion—a partial-variance-of-increments analysis. *The Astrophysical Journal Supplement Series*, *246*(2), 31. Retrieved from https://dx.doi.org/10.3847/1538-4365/ab53d2 doi: 10.3847/1538-4365/ab53d2

Choi, K.-E., Lee, D.-Y., Marubashi, K., & Lee, S. (2022, may). Near-orthogonal orientation of small-scale magnetic flux ropes relative to the background interplanetary magnetic field. *The Astrophysical Journal*, *931*(2), 98. Retrieved from https://dx.doi.org/10.3847/1538-4357/ac69d3 doi: 10.3847/1538-4357/ac69d3

Davis, M. S., Phan, T. D., Gosling, J. T., & Skoug, R. M. (2006). Detection of oppositely directed reconnection jets in a solar wind current sheet. *Geophysical Research Letters*, *33*(19). Retrieved from https://agupubs.onlinelibrary.wiley.com/doi/abs/10.1029/2006GL026735 doi: https://doi.org/10.1029/2006GL026735

Fargette, N., Lavraud, B., Rouillard, A., Eastwood, J. P., Bale, S. D., Phan, T., . . . Bonnell, J. W. (2021). Magnetic increases with central current sheets: observations with parker solar probe. *A&A*, *650*, A11. Retrieved from https://doi.org/10.1051/0004-6361/202039191 doi: 10.1051/0004-6361/202039191

Farooki, H., Lee, J., Pecora, F., Wang, H., & Kim, H. (2024, apr). Axial flux evolution of small-scale magnetic flux ropes from 0.06 to 10 au. *The Astrophysical Journal Letters*, *965*(2), L18. Retrieved from https://dx.doi.org/10.3847/2041-8213/ad3964 doi: 10.3847/2041-8213/ad3964

Farooki, H., Noh, S. J., Lee, J., Wang, H., Kim, H., Abduallah, Y., . . . Pecora, F. (2024, mar). A closer look at small-scale magnetic flux ropes in the solar wind at 1 au: Results from improved automated detection. *The Astrophysical Journal Supplement Series*, *271*(2), 42. Retrieved from https://dx.doi.org/10.3847/1538-4365/ad24e1 doi: 10.3847/1538-4365/ad24e1

Gosling, J. T., & Phan, T. D. (2013, jan). Magnetic reconnection in the solar wind at current sheets associated with extremely small field shear angles. *The Astrophysical Journal Letters*, *763*(2), L39. Retrieved from https://dx.doi.org/10.1088/2041-8205/763/2/L39 doi: 10.1088/2041-8205/763/2/L39

Gosling, J. T., Skoug, R. M., McComas, D. J., & Smith, C. W. (2005). Magnetic disconnection from the sun: Observations of a reconnection exhaust in the solar wind at the heliospheric current sheet. *Geophysical Research Letters*, *32*(5). Retrieved from https://agupubs.onlinelibrary.wiley.com/doi/abs/10.1029/2005GL022406 doi: https://doi.org/10.1029/2005GL022406

Greco, A., Chuychai, P., Matthaeus, W. H., Servidio, S., & Dmitruk, P. (2008). Intermittent mhd structures and classical discontinuities. *GRL*, *35*(19). Retrieved from http://dx.doi.org/10.1029/2008GL035454 (L19111) doi: 10.1029/2008GL035454

Greco, A., Matthaeus, W., Perri, S., Osman, K., Servidio, S., Wan, M., & Dmitruk, P. (2018). Partial variance of increments method in solar wind observations and plasma simulations. *Space Science Reviews*, *214*, 1–27. Retrieved from https://dx.doi.org/10.1007/s11214-017-0435-8 doi: 10.1007/s11214-017-0435-8

Greco, A., Matthaeus, W. H., Servidio, S., Chuychai, P., & Dmitruk, P. (2009, jan). *ApJ*, *691*(2), L111–L114. Retrieved from https://doi.org/10.1088/0004-637x/691/2/l111 doi: 10.1088/0004-637x/691/2/l111

Hasegawa, H., Sonnerup, B. U. O., Owen, C. J., Klecker, B., Paschmann, G., Balogh, A., & Rème, H. (2006). The structure of flux transfer events recovered from cluster data. *Annales Geophysicae*, *24*(2), 603–618. Retrieved from https://angeo.copernicus.org/articles/24/603/2006/ doi: 10.5194/angeo-24-603-2006

Hasegawa, H., Wang, J., Dunlop, M. W., Pu, Z. Y., Zhang, Q.-H., Lavraud, B., ... Bogdanova, Y. V. (2010). Evidence for a flux transfer event generated by multiple x-line reconnection at the magnetopause. *Geophysical Research Letters*, *37*(16), L16101. Retrieved from https://agupubs.onlinelibrary.wiley.com/doi/abs/10.1029/2010GL044219 doi: https://doi.org/10.1029/2010GL044219

Hau, L.-N., & Sonnerup, B. U. Ö. (1999). Two-dimensional coherent structures in the magnetopause: Recovery of static equilibria from single-spacecraft data. *JGR*, *104*(A4), 6899–6917. Retrieved from http://dx.doi.org/10.1029/1999JA900002 doi: 10.1029/1999JA900002

Horbury, OBrien, H., Carrasco Blazquez, I., Bendyk, M., Brown, P., Hudson, R., ... Walsh, A. P. (2020). The solar orbiter magnetometer. *A&A*, *642*, A9. Retrieved from https://doi.org/10.1051/0004-6361/201937257 doi: 10.1051/0004-6361/201937257

Hu, Q. (2017, June). The Grad-Shafranov Reconstruction in Twenty Years: 1996 - 2016. *ScChD*, *60*, 1466-1494. doi: doi:10.1007/s11430-017-9067-2

Hu, Q., He, W., & Chen, Y. (2022). A magnetic flux rope configuration derived by optimization of two-spacecraft in-situ measurements. *Frontiers in Physics*, *10*. Retrieved from https://www.frontiersin.org/articles/10.3389/fphy.2022.960315 doi: 10.3389/fphy.2022.960315

Hu, Q., & Sonnerup, B. U. O. (2000). Magnetopause transects from two spacecraft: A comparison. *GRL*, *27*(10), 1443–1446. Retrieved from http://dx.doi.org/10.1029/1999GL010751 doi: 10.1029/1999GL010751

Hu, Q., & Sonnerup, B. U. Ö. (2001). Reconstruction of magnetic flux ropes in the solar wind. *GRL*, *28*, 467-470. doi: 10.1029/2000GL012232

Hu, Q., & Sonnerup, B. U. Ö. (2002). Reconstruction of magnetic clouds in the solar wind: Orientations and configurations. *JGR*, *107*(A7), 1142. doi: 10.1029/2001JA000293

Hu, Q., Zheng, J., Chen, Y., le Roux, J., & Zhao, L. (2018, November). Automated Detection of Small-scale Magnetic Flux Ropes in the Solar Wind: First Results from the Wind Spacecraft Measurements. *ApJS*, *239*, 12. doi: 10.3847/1538-4365/aae57d

Hu, Q., Zhu, C., He, W., Qiu, J., Jian, L. K., & Prasad, A. (2022, jul). Validation and interpretation of a three-dimensional configuration of a magnetic cloud flux rope. *The Astrophysical Journal*, *934*(1), 50. Retrieved from https://dx.doi.org/10.3847/1538-4357/ac7803 doi: 10.3847/1538-4357/ac7803

Huang, J., Kasper, J. C., Fisk, L. A., Larson, D. E., McManus, M. D., Chen, C. H. K., … Halekas, J. S. (2023, jul). The structure and origin of switchbacks: Parker solar probe observations. *The Astrophysical Journal*, *952*(1), 33. Retrieved from https://dx.doi.org/10.3847/1538-4357/acd17e doi: 10.3847/1538-4357/acd17e

Huang, N., D'Anna, S., & Wang, H. (2023, mar). Statistical study of ejections in coronal hole regions as possible sources of solar wind switchbacks and small-scale magnetic flux ropes. *ApJL*, *946*(1), L17. Retrieved from https://dx.doi.org/10.3847/2041-8213/acc0f1 doi: 10.3847/2041-8213/acc0f1

Kasper, J. C., Abiad, R., Austin, G., Balat-Pichelin, M., Bale, S. D., Belcher, J. W., … others (2016). Solar wind electrons alphas and protons (sweap) investigation: design of the solar wind and coronal plasma instrument suite for solar probe plus. *SSRv*, *204*(1-4), 131–186. Retrieved from https://doi.org/10.1038/s41586-019-1813-z doi: 10.1038/s41586-019-1813-z

Kasper, J. C., Bale, S. D., Belcher, J. W., Berthomier, M., Case, A. W., Chandran, B. D. G., … Schwadron, N. A. (2019). Alfvénic velocity spikes and rotational flows in the near-sun solar wind.

Natur, *576*(7786), 228-231. Retrieved from https://doi.org/10.1038/s41586-019-1813-z doi: 10.1038/s41586-019-1813-z

Klein, K. G., Spence, H., Alexandrova, O., Argall, M., Arzamasskiy, L., Bookbinder, J., ... others (2023). Helioswarm: a multipoint, multiscale mission to characterize turbulence. *Space Science Reviews*, *219*(8), 74. Retrieved from https://link.springer.com/article/10.1007/s11214-023-01019-0 doi: 10.1007/s11214-023-01019-0

Li, G. (2008, jan). Identifying current-sheet-like structures in the solar wind. *The Astrophysical Journal*, *672*(1), L65. Retrieved from https://dx.doi.org/10.1086/525847 doi: 10.1086/525847

Livi, R., Larson, D. E., Kasper, J. C., Abiad, R., Case, A. W., Klein, K. G., ... McManus, M. D. (2022, oct). The solar probe analyzer—ions on the parker solar probe. *ApJ*, *938*(2), 138. Retrieved from https://dx.doi.org/10.3847/1538-4357/ac93f5 doi: 10.3847/1538-4357/ac93f5

Miao, B., Peng, B., & Li, G. (2011). Current sheets from ulysses observation. *Annales Geophysicae*, *29*(2), 237–249. Retrieved from https://www.ann-geophys.net/29/237/2011/ doi: 10.5194/angeo-29-237-2011

Owen, Bruno, R., Livi, S., Louarn, P., Al Janabi, K., Allegrini, F., ... Zouganelis, I. (2020). The solar orbiter solar wind analyser (swa) suite. *A&A*, *642*, A16. Retrieved from https://doi.org/10.1051/0004-6361/201937259 doi: 10.1051/0004-6361/201937259

Paschmann, G., & Daly, P. W. (1998). Analysis methods for multi-spacecraft data. issi scientific reports series sr-001, esa/issi, vol. 1. isbn 1608-280x, 1998. *ISSIR*, *1*.

Pecora, F., Greco, A., Hu, Q., Servidio, S., Chasapis, A. G., & Matthaeus, W. H. (2019, aug). Single-spacecraft identification of flux tubes and current sheets in the solar wind. *ApJ*, *881*(1), L11. Retrieved from https://doi.org/10.3847%2F2041-8213%2Fab32d9 doi: 10.3847/2041-8213/ab32d9

Phan, T. D., Bale, S. D., Eastwood, J. P., Lavraud, B., Drake, J. F., Oieroset, M., ... Velli, M. (2020, feb). Parker solar probe in situ observations of magnetic reconnection exhausts during encounter 1. *ApJS*, *246*(2), 34. Retrieved from https://doi.org/10.3847%2F1538-4365%2Fab55ee doi: 10.3847/1538-4365/ab55ee

Phan, T. D., Drake, J. F., Larson, D., Oieroset, M., Eriksson, S., Yin, Z., ... Raouafi, N. (2024, aug). Multiple subscale magnetic reconnection embedded inside a heliospheric current sheet reconnection exhaust: Evidence for flux rope merging. *The Astrophysical Journal Letters*, *971*(2), L42. Retrieved from https://dx.doi.org/10.3847/2041-8213/ad6841 doi: 10.3847/2041-8213/ad6841

Phan, T. D., Gosling, J. T., & Davis, M. S. (2009). Prevalence of extended reconnection x-lines in the solar wind at 1 au. *Geophysical Research Letters*, *36*(9). Retrieved from https://

agupubs.onlinelibrary.wiley.com/doi/abs/10.1029/2009GL037713 doi: https://doi.org/10.1029/2009GL037713

Phan, T. D., Gosling, J. T., Davis, M. S., Skoug, R. M., Øieroset, M., Lin, R. P., ... others (2006). A magnetic reconnection x-line extending more than 390 earth radii in the solar wind. *Nature*, *439*(7073), 175–178. Retrieved from https://doi.org/10.1038/nature04393 doi: 10.1038/nature04393

Porsche, H. (1981, November). HELIOS mission: Mission objectives, mission verification, selected results. In W. R. Burke (Ed.), *Solar system and its exploration* (Vol. 164, p. 43-50).

Runov, A., Nakamura, R., Baumjohann, W., Zhang, T. L., Volwerk, M., Eichelberger, H.-U., & Balogh, A. (2003). Cluster observation of a bifurcated current sheet. *Geophysical Research Letters*, *30*(2). Retrieved from https://agupubs.onlinelibrary.wiley.com/doi/abs/10.1029/2002GL016136 doi: https://doi.org/10.1029/2002GL016136

Sonnerup, B. U. O., & Guo, M. (1996). Magnetopause transects. *GRL*, *23*(25), 3679–3682. Retrieved from http://dx.doi.org/10.1029/96GL03573 doi: 10.1029/96GL03573

Sonnerup, B. U. O., Hasegawa, H., Teh, W.-L., & Hau, L.-N. (2006). Grad-shafranov reconstruction: An overview. *JGR*, *111*(A9). Retrieved from http://dx.doi.org/10.1029/2006JA011717 (A09204) doi: 10.1029/2006JA011717

Spence, H. E. (2019). Helioswarm: unlocking the multiscale mysteries of weakly-collisional magnetized plasma turbulence and ion heating. In *Agu fall meeting abstracts* (Vol. 2019, pp. SH11B–04). Retrieved from https://ui.adsabs.harvard.edu/abs/2019AGUFMSH11B..04S/abstract

Stansby, D., Salem, C., Matteini, L., & Horbury, T. (2018). A new inner heliosphere proton parameter dataset from the helios mission. *Solar physics*, *293*, 1–11. Retrieved from https://doi.org/10.1007/s11207-018-1377-3 doi: 10.1007/s11207-018-1377-3

Teh, W.-L. (2018). Grad–shafranov reconstruction of magnetohydrostatic equilibria with nonisotropic plasma pressure: the theory. *EP&S*, *70*(1), 1–5. Retrieved from https://doi.org/10.1186/s40623-018-0802-z doi: 10.1186/s40623-018-0802-z

Teh, W.-L., Sonnerup, B. U. O., Hu, Q., & Farrugia, C. J. (2009). Reconstruction of a large-scale reconnection exhaust structure in the solar wind. *Annales Geophysicae*, *27*(2), 807–822. Retrieved from https://angeo.copernicus.org/articles/27/807/2009/ doi: 10.5194/angeo-27-807-2009

Wood, B. E., Hess, P., Chen, Y., & Hu, Q. (2023, aug). Sequential small coronal mass ejections observed in situ and in white-light images by parker solar probe. *The Astrophysical Journal*, *953*(2), 123. Retrieved from https://dx.doi.org/10.3847/1538-4357/ace259 doi: 10.3847/1538-4357/ace259

Zheng, J., & Hu, Q. (2018, January). Observational Evidence for Self-generation of Small-scale Magnetic Flux Ropes from Intermittent Solar Wind Turbulence. *ApJL*, *852*, L23. doi: 10.3847/2041-8213/aaa3d7